




Type II porous ionic liquid based on metal-organic cages that enables L-tryptophan identification

Zhuxiu Zhang ¹, Baolin Yang¹, Bingjie Zhang¹, Mifen Cui¹, Jihai Tang ^{1,2}✉ & Xu Qiao ^{1,2}✉

Porous liquids with chemical separation properties are quite well-studied in general, but there is only a handful of reports in the context of identification and separation of non-gaseous molecules. Herein, we report a Type II porous ionic liquid composed of coordination cages that exhibits exceptional selectivity towards L-tryptophan (L-Trp) over other aromatic amino acids. A previously known class of anionic organic-inorganic hybrid doughnut-like cage (HD) is dissolved in trihexyltetradecylphosphonium chloride (THTP-Cl). The resulting liquid, HD/THTP-Cl, is thereby composed of common components, facile to prepare, and exhibit room temperature fluidity. The permanent porosity is manifested by the high-pressure isotherm for CH₄ and modeling studies. With evidence from time-dependent amino acid uptake, competitive extraction studies and molecular dynamic simulations, HD/THTP-Cl exhibit better selectivity towards L-Trp than other solid state sorbents, and we attribute it to not only the intrinsic porosity of HD but also the host-guest interactions between HD and L-Trp. Specifically, each HD unit is filled with nearly 5 L-Trp molecules, which is higher than the L-Trp occupation in the structure unit of other benchmark metal-organic frameworks.

¹ State Key Laboratory of Materials-Oriented Chemical Engineering, College of Chemical Engineering, Nanjing Tech University, No. 30 Puzhunan Road, 211816 Nanjing, China. ² Jiangsu National Synergetic Innovation Centre for Advanced Materials (SICAM), No. 5 Xinmofan Road, 210009 Nanjing, China.
✉email: jhtang@njtech.edu.cn; qct@njtech.edu.cn

Porous liquids represent an emerging class of materials that combine the benefits of porosity and fluid properties in a rational manner^{1–3}. The intrinsic porosities of porous liquids are mainly derived from components with either zero dimensional nanostructures (e.g. molecular cages⁴, hollow silica⁵) or extended network structures (e.g. metal-organic frameworks⁶ and zeolites⁷). Their modular nature and structure diversity facilitate the exquisite control over porous liquids with respect to the pore size and chemistry through the judicious selection of structural constituent. Such versatile porosities thereby enable systematic studies that afford an understanding of structure-function relationships of porous liquids, which has led them to be of particular interest for potential utility in gas storage^{8–16}, separations^{17–20} and catalysis^{21–23}.

More than one third of pore liquids consist of molecular cages including porous organic cages (POCs) and metal-organic cages (MOCs) as pore hosts. Molecular cages are generally solid state materials at atmospheric condition. The functionalization of their periphery with alkyl chains^{24,25} or poly(ethylene glycol) chains⁴ offers opportunities to reduce the melting point, giving rise to the Type I porous liquids. Another synthetic approach of Type I porous liquids is to transform the anionic POC into ionic liquid by pairing with cationic 18-crown-6/ K^+ complex²⁶. However, most of molecular cage-derived porous liquids are generated via dissolving molecular cages in bulky solvents, also known as Type II porous liquids. The dissolution process is essentially simpler than multi-step organic synthesis involved in the synthesis of Type I porous liquids. MOCs^{27–29} are an important class of discrete nanoscale structures amenable to crystal engineering^{30,31} and can be rationally designed using the ‘node-and-spacer’ approach. The pre-selection of nodes and spacers enables the fine-tuning of structure and properties, so that MOCs can be regarded as ideal pore hosts for Type II porous liquids. In fact, MOCs have been explored in liquid phase to extract target molecules from another immiscible liquid phase via host-guest binding affinity³². There is also a handful of papers regarding the gas encapsulation in cavities of MOCs in solution³³. However, the use of volatile solvent and the unwanted occupation of the cage cavity fails to endow the solution of MOCs with permanent porosity. To our knowledge, there is only one MOC-based Type II porous liquid generated by dissolving MOP-18 in 15-crown-5¹⁸. In this contribution, we introduce a class of Type II porous liquids composed of anionic organic–inorganic hybrid doughnut-like nanostructures (HD)³⁴ dissolved in trihexyltetradecylphosphonium chloride (THTP-Cl). Note that this is also an underexplored example of Type II porous ionic liquid based upon MOCs.

Molecular cages, including those serve as the “doughnut-shaped” host (e.g. cyclodextrin and cucurbiturils), have been of particular interest in the contemporary supramolecular chemistry³⁵. Porous liquids consisting of molecular cages thereby exhibit host-guest properties, as exemplified by the shape and size selectivity for a series of isomeric alcohols in Type I porous ionic liquids composed of tetrahedral coordination cage⁴. Most recently, Xia et al. reported the use of the cyclodextrin-derived Type I porous liquid for the efficient chiral recognition and separation of nucleosides in the solution³⁶. Except for the two examples above, current research on the host-guest properties of the molecular cage-based porous liquids has been mainly focused on the accommodation of small gaseous molecules such as carbon dioxide^{8,37,38}, methane^{11,14,39} and chlorofluorocarbon⁴. It still remains a rare and poorly understood the capture of non-gaseous guest molecules in porous liquids. The downstream processing of naturally derived amino acids include chromatographic steps for the separation and purification of amino acids. Porous solids such as ion-exchange resin have been used for the chromatographic separation of amino acid, which necessarily entail batch

operations that accounts for 80% of the amino acid cost. Hence, there is a critical need to develop alternative selective separation process for amino acids with high purity and low cost.⁴⁰ Against the greatly explored batch or semi-batch processes involving multiple energy-intensive unit operations, the continuous production scheme which promise much higher productivity and higher acid concentration can be considered good alternatives⁴¹. In this context, the use of the porous liquid as the porous extraction medium, which has the potential to be incorporated in the continuous flow process⁴², is likely to generate versatile platforms for the isolation and purification of amino acid from the fermentation broth.

In this work, we report the use of the Type II porous ionic liquid (HD/THTP-Cl) based upon anionic organic–inorganic hybrid doughnut-like cage for the selective extraction of L-tryptophan (L-Trp) from the aromatic amino acid mixtures in aqueous solution. HD/THTP-Cl is characterized by several techniques covering the key properties including the thermal properties, rheological properties, permanent porosity and viscosity. HD/THTP-Cl exhibits not only higher L-Trp selectivity than other typical porous liquids but also larger unit occupation of L-Trp than other benchmark porous coordination polymers. We attribute such exceptional performance to the intrinsic porosity of HD and exceptional L-Trp binding affinity as revealed by modeling studies. The synthetic approach of HD/THTP-Cl can be extended to a broad family of metal-organic cages. The use of HD/THTP-Cl as the task-specific extractant represent a broad paradigm to target the selectivity towards other biomolecules as exemplified by the selective extraction of D-ribose from the aqueous solution of D-ribose and D-glucose.

Result and discussion

Synthesis and purification. The crystallization of anionic organic–inorganic hybrid nanodoughnut (HD) with dimethylammonium (DMA) as the counter-ion occurs during the solvothermal reaction of 5-bromo-1,3-benzenedicarboxylic acid and VCl_3 in DMF. The resulting DMA_4 -HD crystals are difficult to be dissolved in organic solvents (e.g. 15-crown ether and hexachloropropene) that have been used for the synthesis of Type II porous liquids, because DMA_4 -HD is essentially a type of salt difficult to be ionic dissociated in the aprotic organic solvent. Attempts dissolve DMA_4 -HD in imidazole/pyridine/ammonium-based ionic liquids were unsuccessful. Fortunately, we observed the readily dissolution of DMA_4 -HD in trihexyltetradecylphosphonium chloride (THTP-Cl) to form the dark green liquid (DMA_4 -HD/THTP-Cl) via stirring at room temperature (Fig. 1a). THTP-Cl is a branched ionic liquid of which the branched topology and molecular size can prevent itself from entering the nano-sized pores⁴³. It's necessary to remove DMA from DMA_4 -HD/THTP-Cl because it may occupy the cavity of HD in the solution. The addition of acetonitrile to DMA_4 -HD/THTP-Cl formed a certain amount of the white precipitate with the melting point (T_m) of 173 °C corresponding to the pure dimethylammonium chloride (Fig. 1b). The bulk purity of the precipitate was furtherly verified by comparing its X-ray powder diffraction pattern with commercialized dimethylammonium chloride (Fig. 1c). The content of C, H and N in precipitate was respectively verified as 28.83%, 9.32% and 17.03% via elemental analysis (Calculated: C 29.45%; H 9.88%; N 17.17%). The presence of methyl group in the white precipitate was determined by ¹H NMR analysis (Supplementary Fig. 1). Thus, the white precipitate can be verified as the pure dimethylammonium chloride. The molar ratio of DMA and HD in DMA_4 -HD/THTP-Cl was calculated through the moles of white precipitate divided by the moles HD in HD/THTP-Cl. Considering the inevitable small

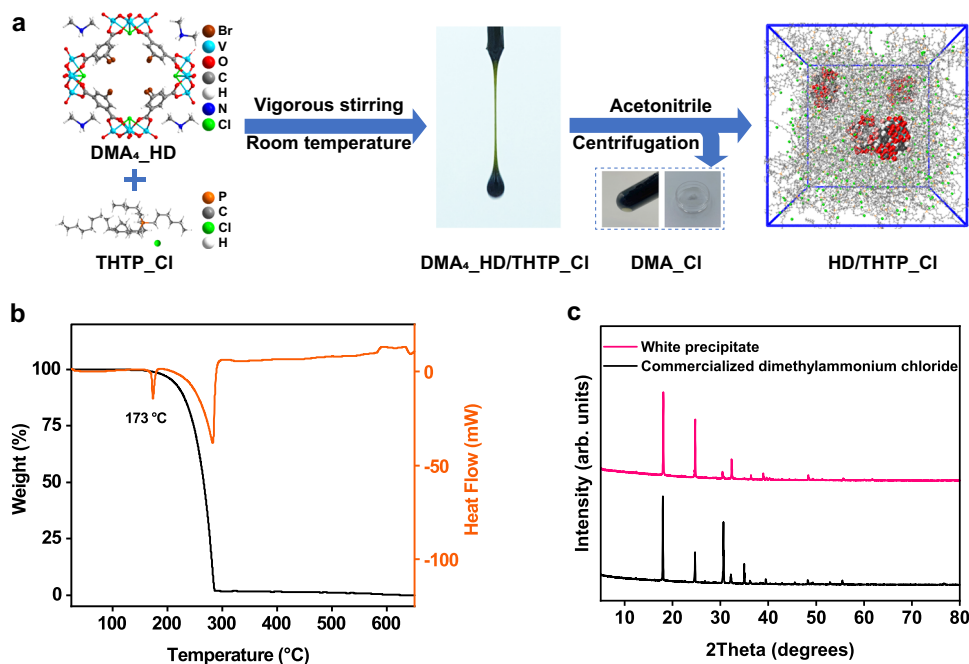


Fig. 1 Synthesis of HD/THTP-Cl and characterization of the removed white precipitate characterization. **a** Schematic illustration of the synthesis of HD/THTP-Cl. **b** TG-DSC curve of the white precipitate. **c** Experimental PXRD pattern of the white precipitate and commercialized dimethylammonium chloride.

amount of weight loss during the purification, we think the resulting molar ratio of 3.85:1 is consistent with the molecular formula of as-synthesized DMA₄-HD. To be specific, the dark green liquid (DMA₄-HD/THTP-Cl, 5.55 g) contains 0.1 mmol of DMA₄-HD and 10 mmol of THTP-Cl. It thereby needs 0.4 mmol of Cl⁻ anions from THTP-Cl to form dimethylammonium (DMA-Cl). Once the DMA-Cl was removed by adding acetonitrile, the remaining liquid contains 0.1 mmol of HD⁴⁻ anions, 9.6 mmol of Cl⁻ anion and 10 mmol of THTP⁺ cation. The charge of the liquid was thereby balanced.

Structural characterization. The quadrupole time-of-flight (QTOF) mass spectrum of the HD/THTP-Cl in acetonitrile confirms the existence of HD anion, according to the peaks at the *m/z* of 853.2508 assigned to the molecular formula of [(V₄O₈Cl)₄(C₈H₃BrO₄)₈]⁴⁻. Another intense molecular ion peaks at the *m/z* of 483.5105 are assigned to THTP cation, [C₃₂H₆₈P]⁺ (Fig. 2a). There are no powder X-ray diffraction peaks of HD/THTP-Cl compared to as-synthesized DMA₄-HD, excluding the existence of small HD crystallites dispersed in the liquid (Fig. 2b). All HD anions are fully dissolved in the THTP-Cl as indicated by dynamic light scattering measurements with an average size of 1.8 nm, which is in good agreement with diameter of HD cage (Fig. 2c). Thermogravimetric analysis reveals a similar thermal stability between HD/THTP-Cl and THTP-Cl before decomposition (Supplementary Fig. 2). Differential scanning calorimetry (DSC) curves showed an endothermic/exothermic peaks of HD/THTP-Cl and THTP-Cl of -64.42/-70.05 and -68.51/-72.71 °C respectively, corresponding to the melting temperature (*T_m*) and crystallization temperature (*T_c*). HD/THTP-Cl and THTP-Cl exhibited a similar thermal hysteresis behavior related to the reversible first-order structural phase transition⁴⁴. Both *T_m* and *T_c* of HD/THTP-Cl are slightly higher than those in THTP-Cl, which can be tentatively attributed to inhibition of both chains mobility and vibration of THTP cations by HD anions⁴⁵ (Fig. 2d).

The rheological properties of HD/THTP-Cl were studied by a rotational rheometer. The frequency sweeps were conducted

within a linear viscoelastic region between 0.1% and 1% from an initial amplitude sweep (Fig. 2e inset). The liquid-like behavior is reflected by higher loss modulus (*G''*) than storage modulus (*G'*) at low angular frequency range. The equivalent modulus value indicates the solid-liquid transition of HD/THTP-Cl at an angular frequency of 39.8 rad/s (Fig. 2e). HD/THTP-Cl shows the evidence of Newtonian fluid as the linear dependence of shear stress on the shear rate (Supplementary Fig. 3). The viscosity of HD/THTP-Cl thereby remain invariant of 0.7 Pa-s with increasing shear rate (Supplementary Fig. 4), and it was even lower than the viscosity of pure THTP-Cl at 25 °C (1 Pa-s) (Fig. 2f).

Demonstration of porosity in HD/THTP-Cl. Molecular Dynamics (MD) simulations of a bulk system consisting of 5 HD anions, 500 THTP cations and 480 chloride anions in a cubic and periodic simulation box were carried out in the NPT ensemble at 1 bar and 298 K with a time-step of 2 fs. To estimate the energy barrier for THTP cations and chloride anions transporting through the HD anion, the potential of mean force (PMF) was studied via radial distribution functions. The approaching of THTP cations and chloride anions to HD causes the significant increase of PMF from 0 to 12.5 kJ/mol, so that the minimum distance between HD and chloride anions are at approximately 0.8 nm (Fig. 3a). In contrast, the distance between HD anion and THTP cation can be as close as approximately 0.45 nm, which is consistent with the larger interaction energy of 120 kJ/mol than that of 50 kJ/mol between HD anion and chloride anion due to electrostatic repulsion (Fig. 3b). On average, around 100% of the THTP cations at any given time are outside the HD anions so that there is enough void cavities in HD/THTP-Cl (Fig. 3c).

The MD simulation result detailed herein prompted us to evaluate the high-pressure CH₄ absorption ability of HD/THTP-Cl from 0 to 65 bar, and THTP-Cl was also chosen as the contrast. The gravimetric CH₄ uptakes (298 K, 65 bar) in HD/THTP-Cl and THTP-Cl are 0.28 and 0.18 mmol/g respectively (Fig. 3d). We then carried out a simulation of the 1:100:96 mixture of HD, THTP and chloride ions combined with 100

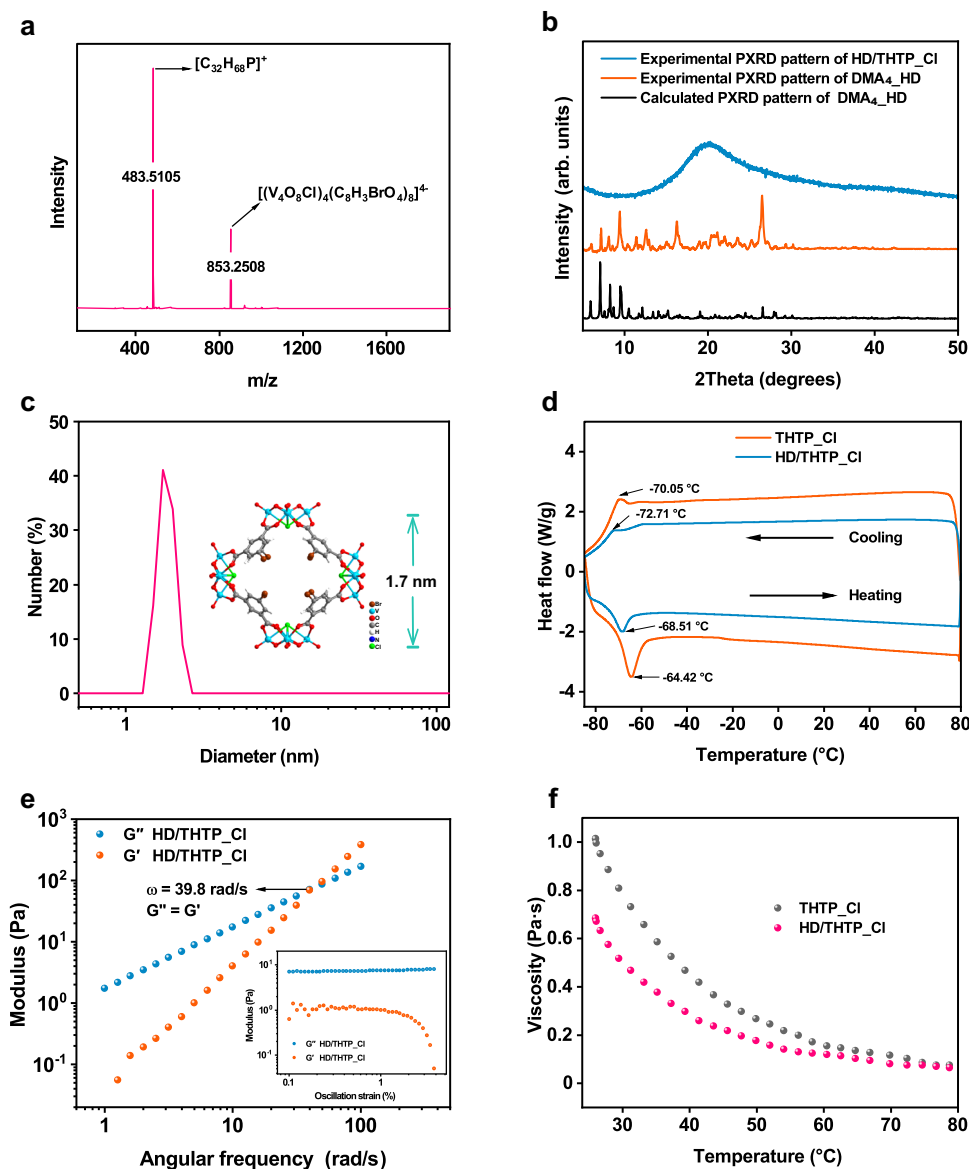


Fig. 2 Structure characterizations of HD/THTP_Cl. **a** QTOF mass spectrum of HD/THTP_Cl. **b** Experimental PXRD patterns of DMA₄HD and HD/THTP_Cl, and calculated PXRD pattern of DMA₄HD. **c** Particle size and distribution from DLS measurements of HD/THTP_Cl in acetonitrile. Inset: Molecular structure of HD anion with the diameter of 1.7 nm. **d** DSC cooling and successive heating curves of THTP_Cl and HD/THTP_Cl. **e** Frequency-dependent modulus plots of HD/THTP_Cl. Inset: Strain-dependent modulus plots of HD/THTP_Cl with the angular frequency fixed at 5 rad/s. **f** Viscosity-temperature curves of THTP_Cl and HD/THTP_Cl.

methane molecules at 1, 5 and 10 bars, respectively. The starting configuration was generated by randomly placing 100 methane molecules in the bulk fluid without any atomic overlaps. The system was then relaxed for 10 ns under NPT conditions, and all methane molecules were observed freely flowed in HD/THTP_Cl during the simulations. Supplementary Fig. 5 shows the number of methane molecules residing in the HD cavity as a function of time during the production run. The average number of methane molecules residing in HD cavity derived from MD simulation and the number of methane molecules encapsulated by HD cavity calculated from high-pressure methane absorption data were listed in Supplementary Table 1. It is interesting to find that simulated number of methane molecules is higher than the experimental ones at pressure from 1 to 10 bar. The higher the pressure, the closer the experimental number of methane molecules towards the simulated number. In this case, we tentatively attribute this phenomenon to the limited mass transfer

of methane molecules in the viscous porous liquid. The viscosity of HD/THTP_Cl was 0.7 Pa·s at 25 °C, which was nearly 700 times larger than the viscosity of water. Thus, the mass transfer of methane molecules in HD/THTP_Cl at low pressure is supposed to be reduced⁴⁶. In contrast, the high pressure is likely to provide stronger driving force for the methane molecules to move into the HD cavity⁴⁷. This is the reason why the simulated and experimental number of methane molecules are quite close at 65 bar. There are on average 4.72 methane molecules residing in the HD cavity at 65 bar according to the MD simulations, which means the number of methane molecules in the HD cavity kept fluctuating during simulation process. Figure 3e presents the simulation systems at the running time of 10 ns, where there are exactly 4 methane molecules encapsulated in the HD cavity. According to Supplementary Fig. 5d, other running times around 10 ns may exhibit the simulation system containing 3 or 5 methane molecules encapsulated in the HD cavity.

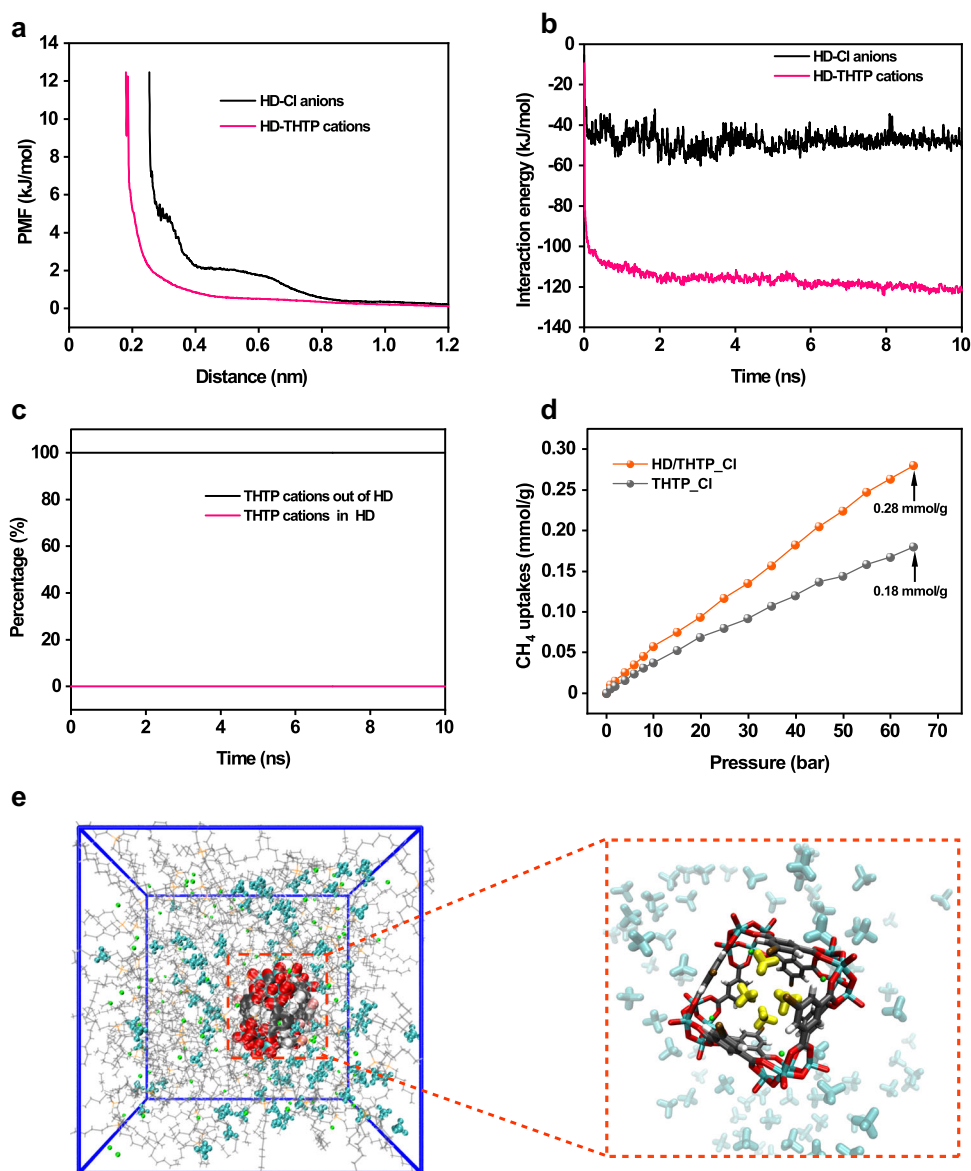


Fig. 3 Porosity measurements. **a** Center-of-mass—a-particular-atom PMF for HD –THTP cations (P atom) and HD-Cl anions (Cl atom) from MD simulations. **b** The interaction energy of HD anion with THTP cation and chloride anion. **c** Simulated distribution percentage of THTP cation in and out of the cavity of HD. **d** High-pressure CH_4 absorption data of HD/THTP_Cl and THTP_Cl. **e** The simulation box of methane in HD/THTP_Cl at 25 °C and 65 bar, in which the HD anion is occupied by four methane molecules at 10 ns. (Methane molecule inside and outside of HD are respectively highlighted with yellow and cyan).

Selective extraction of L-tryptophan from aromatic amino acids mixture.

L-Tryptophan (L-Trp) is one of the eight essential amino acids that play a key role in human metabolism as exemplified by the biosynthesis of neurotransmitters, hormones, and vitamins. The isolation and purification of L-Trp from the fermentation broth that contains L-tyrosine (L-Tyr) and L-phenylalanine (L-Phe) as major impurities is an important for the L-Trp production. Liquid–liquid extraction is one of the widely used separation methods, and experiments were carried out by allowing 0.1 mL of HD/THTP_Cl come into contact with 2 mL of aqueous solution of amino acid. The concentration of L-Trp, L-Tyr and L-Phe is 0.05 mol/L, 0.15 mol/L and 0.002 mol/L respectively. All three concentrations are close to the maximum concentrations of corresponding amino acids⁴⁸. For the single-component system, Fig. 4a presents a significant increase of the extraction rate before equilibrium as indicated by the incremental concentration of L-Trp in the HD/THTP_Cl phase during the timeframe of 1–4 h. The extraction

reached equilibrium at 8 h as exhibited by the plateau from kinetic curves, and the final L-Trp uptake was 108.2 $\mu\text{mol/g}$ after 24 h. Comparably, the extraction ability of THTP_Cl was significantly reduced to 17.7 $\mu\text{mol/g}$ over the whole extraction time range. In addition, neither L-Tyr nor L-Phe was extracted by HD/THTP_Cl or THTP_Cl after 24 h (Supplementary Figs. 6, 7). The reuse of HD/THTP_Cl were realized by adding ethanol/water solution (1:4) for back extraction, followed by being vacuum dried at 60 °C for 2 h. Figure 4b shows that HD/THTP_Cl does not lose its extraction ability after 5 extraction cycles. We have compared the uptake of amino acids in HD/THTP_Cl with other four typical porous liquids in literatures, and none of them exhibited considerable selectivity towards L-Trp. Both of Type III porous liquids use phosphonium-based ionic liquid as the solvent. ZIF-8/THTP_Cl⁴⁹ exhibited similar L-Trp uptake as in HD/THTP_Cl, but the L-Tyr uptake in ZIF-8/THTP_Cl is close to L-Trp. The L-Trp uptake in HZSM-5/THTP_Br⁴³ is four times lower than HD/THTP_Cl probably

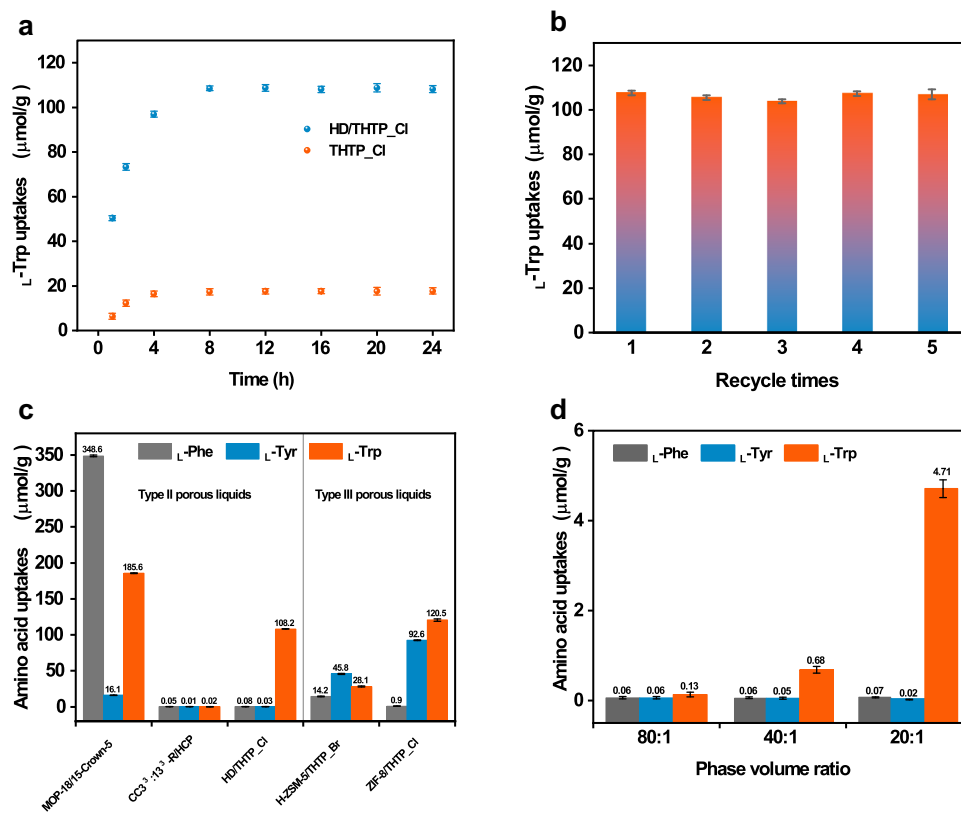


Fig. 4 Selective extraction of L-Trp. **a** L-Trp uptake over time in HD/THTP_Cl and THTP_Cl. **b** The reuse of HD/THTP_Cl for the single-compound extraction of L-Trp. **c** The uptake of amino acids in MOP-18/15-crown-5, CC3³:13³-R/HCP, HD/THTP_Cl, H-ZSM-5/THTP_Br and ZIF-8/THTP_Cl. **d** Effect of the phase volume ratio on the L-Trp selectivity.

because of its narrow pore size, and the uptake of L-Phe and L-Tyr is also highly reduced too. The CC3³:13³-R/HCP¹⁴ is Type II porous liquid based upon porous organic cage dissolved in hexachloropropene, but its ultra-microporosity resulted in the negligible uptake of all three amino acids. MOP-18/15-Crown-5¹⁸ is another Type II porous liquid based upon metal-organic cage, and it showed considerable uptake of L-Trp (185.6 μmol/g) and L-Phe (348.6 μmol/g) (Fig. 4c and Supplementary Table 3). Therefore, only HD/THTP_Cl exhibited the selectivity towards L-Trp.

To support and confirm the high selectivity derived from the single-component extraction experiments, the selective L-Trp extraction by HD/THTP_Cl from the model solution that contains equimolar mixture of L-Trp, L-Tyr and L-Phe was investigated and presented in Fig. 4d. The initial concentration of each amino acid in water phase is 2 mmol/L with the water: HD/THTP_Cl phase ratio of 20:1, and higher phase ratio means lower initial concentration of amino acids. Both concentrations of L-Tyr and L-Phe are close to zero at phase volume ratio of 80:1, 40:1 and 20:1. The concentration of L-Trp in aqueous phase after extraction is 0.1 mmol/L at the phase volume ratio of 80:1. When the phase volume ratio increase to 20:1, the corresponding concentration of L-Trp in water after extraction is 1.7 mmol/L. The separation factor is 24 for L-Trp to L-Phe and 23 for L-Trp to L-Tyr at the phase ratio of 20:1, whereas the corresponding separation factor are reduced to 0.94 and 0.93 at the phase ratio of 80:1. These results suggest that L-Trp can be selectively separated from a mixture of amino acids by HD/THTP_Cl, and the use of low phase volume ratios, such as 20:1, is beneficial to the high extraction selectivity.

The high selectivity toward L-Trp exhibited by HD/THTP_Cl is then addressed through molecular dynamic simulations in which amino acid molecules is added in the simulation box for probing

the recognition ability of HD. The simulation system containing L-Trp molecules reach stability within 1 ns and remain stable for the rest simulation time. In comparison, the more fluctuated higher root mean square deviations (RMSD) value of L-Phe and L-Tyr simulation system were found within 2 ns and 3.5 ns, indicating the highly bias and instability of the simulation systems (Supplementary Figs. 8–10 and Supplementary Table 2). There is one L-Trp molecule encapsulated in the cage of HD and four L-Trp molecules surrounding the periphery of HD cage (Fig. 5a). Noncovalent interactions between L-Trp molecule and HD were determined using reduced density gradient (RDG) analysis⁵⁰. The RDG isosurface is colored according to the value of $\text{sign}(\lambda_2)\rho$ to distinguish the different weak interactions, and the interaction type is illustrated by the blue-green-red scale (blue: strong absorption including hydrogen bond and strong halogen bond, green: van der Waals interactions, red: steric hindrance) (Fig. 5b–e and Supplementary Fig. 11). The van der Waals interaction and C–H... π interactions ($d[\text{C}\cdots\text{centroid}_{\text{phen}}] = 4.2 \text{ \AA}$) between the encapsulated L-Trp and HD cage can be clearly detected according to the dispersed low density isosurfaces between L-Trp and the benzene ring of ligand (Supplementary Figs. 12–14). For L-Trp molecules outside the HD cage, the isosurface lies between the nitrogen atom from the indole ring and oxygen atom from the HD cage, indicating several N–H...O interactions with (N...O) distances ranging from 2.4 to 3.4 Å and N–H...O angle ranging from 104° to 158°. RDG analysis also demonstrates that there are several van der Waals interactions between L-Trp and HD cage (Supplementary Figs. 15–18). For MD simulation system containing L-Tyr molecules, there are two L-Tyr molecules surrounding the periphery of HD cage. The N–H...O interaction between amine groups of one L-Tyr and terminal oxygen from HD cage was observed with distance

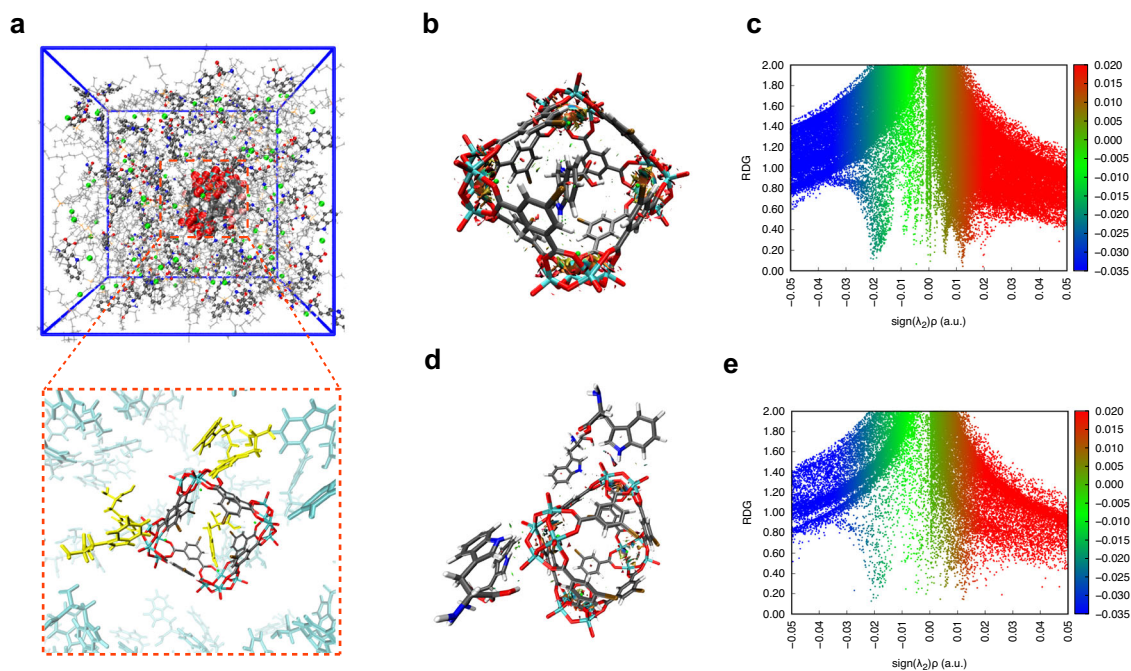


Fig. 5 The L-Trp recognition ability of HD. **a** The simulation box of L-Trp in HD/THTP_Cl, in which the one molecule resides in the cavity of HD and four molecules interact with polyoxovanadates of HD. (The identified L-Trp molecule are respectively highlighted with yellow.) **b** Color-filled RDG isosurfaces depicting noncovalent interaction regions of the encapsulated-L-Trp and HD cage. **c** Plots of $\text{sign}(\lambda_2)\rho$ and its reduced density gradient for the encapsulated-L-Trp and HD cage. **d** Color-filled RDG isosurfaces depicting noncovalent interaction regions of the absorption of L-Trp by the periphery of HD cages. **e** Plots of $\text{sign}(\lambda_2)\rho$ and its reduced density gradient for the absorption of L-Trp by the periphery of HD cages.

(N...O) of 3.2 Å and N-H...O angle of 153°. Similar interactions were found for another L-Tyr molecule with a distance (N...O) of 3.4 Å and N-H...O angle of 167° (Supplementary Figs. 19–21). For MD simulation system containing L-Phe molecules, there is no observable interatomic contacts among L-Phe molecules and HD cages. The shortest distance between L-Phe and adjacent HD cage is 3.9 Å from nitrogen atoms in L-Phe and terminal oxygen atom in HD, which falls out of the range of hydrogen bond (Supplementary Figs. 22, 23). The structural consequence of weak interaction analysis is that the cavity of HD only exhibited favorable interaction with L-Trp, and N-H...O interaction for the periphery of HD cage for L-Trp is on average stronger than L-Tyr as indicated by the bond distance and bond angle.

Except for the intermolecular interaction, the energy barrier for the amino acid transporting through the HD cage is another factor for the extraction selectivity. The potential of mean force (PMF) was investigated to estimate such energy barrier. The approaching of L-Tyr and L-Phe to HD both cause the significant increase of PMF above 100 kJ/mol, so that the minimum distance between HD and L-Tyr/L-Phe is at approximately 0.3 nm. In contrast, the distance between HD anion and THTP cation can be less than 0.15 nm before the sharp increase of PMF. Moreover, the presence of THTP cation is also important for the exclusion of L-Tyr and L-Phe (Supplementary Fig. 24). We calculated binding energy of amino acids with THTP and HD cage respectively. The binding energy of THTP/L-Trp blend was greater than that of THTP/L-Tyr blend and THTP/L-Phe blend, indicating the stronger compatibility of THTP and L-Trp than that of THTP and L-Tyr or L-Phe. THTP itself is likely to extract more L-Trp molecules than L-Phe and L-Tyr, which is consistent with the experiment result. Importantly, the binding energy of HD/L-Trp blend is ca. 19 kJ/mol larger than THTP/L-Trp blend, whereas the binding energy of HD/L-Phe blend is close to that of THTP/L-Phe (Supplementary Table 4). This result further proved that the

presence of HD in THTP_Cl effectively facilitate the affinity of L-Trp for HD rather than L-Phe and L-Tyr.

As with the experimental and modeling results discussed above, L-Trp molecules were not only encapsulated in almost all of the internal cavities of HD/THTP_Cl, but also interacting with the periphery of HD. The number of L-Trp loaded per HD cage unit was calculated to be 4.7. Although the gravimetric uptake of L-Trp in HD/THTP_Cl is moderate by the standard of porous materials⁵¹, the unit occupation of HD/THTP_Cl is unprecedented, outperforming other benchmark porous coordination polymers: 1.3 for UiO-66, 0.4 for MIL-140B, 2.1 for MIL-140C, 1.5 for MIL-140D, 2.2 for MOF-808, 2.6 for MIL-68(Al) and 2.7 for zeolite HY calculated via multiplying the gravimetric uptake of L-Trp by the molecular weight contained in one unit cell of certain MOF (Supplementary Fig. 25). The low unit occupation by L-Trp observed in these porous coordination polymers may originate from two factors: (i) limited access of the L-Trp in narrow pore environment. Adsorbents such as UiO-66 have narrow channel (5–11 Å) that are comparable to the L-Trp dimension (11.1 × 6.4 × 8.1 Å) calculated by Multiwfn program⁵², so that the penetration of the L-Trp might be restricted; (ii) restricted diffusion of the L-Trp to the inner structure. The growth of the MOF or zeolite crystalline particle inevitably resulted in the significant mass transfer resistance since the large particles have a prolonged internal diffusion pathway, thus providing barrier for the penetration of the adsorbate deeper into the adsorbent structure⁵³. In contrast, HD cages are readily accessible to L-Trp, so that there is no side effect of internal diffusion in HD because it is the zero-dimensional structures highly dispersed in the THTP_Cl.

Generality of MOC-based Type II porous ionic liquid. We successfully extended the synthetic protocol to several representative MOCs. Specifically, six vanadium-based anionic

MOCs, three zirconium-based cationic MOCs and two copper-based neutral MOCs were selected as pore hosts for the synthesis of various porous liquids under the same procedures. All selected MOCs are typical because they follow one of the three design principles including vertex-directed, face-directed and edge directed self-assembly, which afford MOCs with windows and faces, faces only or windows only, respectively. The details of all selected MOCs were listed in Supplementary Table 5. It is interesting to find that all charged MOCs can be readily dissolved in THTP_Cl, whereas both copper-based neutral MOCs exhibit poor solubility in THTP_Cl. The maximum solubility of each MOC in THTP were listed in Supplementary Table 5. The presence of MOCs after the dissolution into THTP_Cl were verified by QTOF-MS test for charged MOCs and MALDI-TOF test for neutral MOCs (Supplementary Fig. 26). The permanent porosities of all porous liquids were verified by the high-pressure methane uptakes which are all larger than THTP_Cl due to the occupation of methane molecules in MOCs. The uptake difference among all these MOC-based porous liquids are related to the concentration of MOCs in THTP_Cl and the pore size/volume of MOCs (Supplementary Fig. 27). As presented in Supplementary Table 5, all porous liquids exhibit observable fluidity, and the color of porous liquid is derived from the MOCs.

HD/THTP_Cl has been demonstrated to selectively extract L-Trp from aromatic amino acids mixture. We envisioned that HD/THTP_Cl can be extended to target the selectivity toward other biomolecules by utilizing the intrinsic cavity in HD/THTP_Cl. D-Ribose has been produced by microbial fermentation of D-glucose which are abundant in lignocellulosic biomass. The isolation and purification of D-ribose from fermentation broth is an important step during the whole fermentation process. In a typical experiment, the aqueous solution of equimolar D-ribose over D-glucose (2.5 mmol/L, 2 mL) was contacted with HD/THTP_Cl (0.1 mL). The mixture was stirred vigorously for 8 h at room temperature. The D-ribose uptake in HD/THTP_Cl (38.2 $\mu\text{mol/g}$) was much higher than pure THTP_Cl (5.5 $\mu\text{mol/g}$), and the number of D-ribose loaded per HD cage unit was calculated as 1.8. In contrast, the D-glucose uptake in pure THTP_Cl (5.3 $\mu\text{mol/g}$) was very close to HD/THTP_Cl (5.9 $\mu\text{mol/g}$), indicating the infeasible encapsulation of D-glucose in the HD cavity. These results suggest that D-ribose can be selectively extracted from the aqueous solution of D-ribose and D-glucose by HD/THTP_Cl. HD/THTP_Cl thereby has the potential to serve as the porous extraction media to isolate D-ribose in the preparative course.

In summary, HD/THTP_Cl is a Type II porous ionic liquid based upon coordination cages that induces a non-gaseous guest molecules selectivity. The modeling and several experimental studies provide structural insight into the existence of the permanent porosity in THTP_Cl with 6% HD. Compare with pure THTP_Cl, we have demonstrated how the empty cavity of HD, coupled with favorable host-guest interactions provided by the internal chemical environment of HD cage, affords HD/THTP_Cl with exceptional selectivity and recyclability in the context of industrially relevant L-Trp separation applications. Furthermore, the unit occupation by L-Trp in HD/THTP_Cl is much higher than other benchmark solid state porous material thanks to the pore size and dissolution of HD that enhance the diffusion of the L-Trp molecules into the intrinsic pores of HD/THTP_Cl. Perhaps most importantly, HD belongs to one of the most extensively studied and broadest classes of polyoxovanadate-based coordination cages⁵⁴ and is therefore likely to serve as prototypical to promote a platform of related porous liquid with potential to resolve industrial challenges related to molecular separation.

Methods

Synthesis of DMA₄-HD. According to the previously reported procedure³⁴, a mixture of 5-bromo-1,3-benzenedicarboxylic acid (12.0 mg), VCl₃ (20.0 mg) and 5 mL mixture solvent (DMF: H₂O = 10:1) were put in a 20 mL scintillation vials and heated to 105 °C for 3 days until dry. The resulting residue were dissolved in DMF and dark green block crystals were obtained by slow diffusion of diethyl ether. Crystals were washed with menthol to give pure DMA₄-HD of 16.3 mg (yield of 46% based on the ligand). Elemental analysis calculated: C 27.38%; H 2.87%; N 4.47%; Experimental: C 26.48%; H 2.94%; N 4.53%. IR (KBr, cm⁻¹): 3448 (br), 2783 (w), 1719 (m), 1603 (m), 1543 (s), 440 (s), 1409 (w), 1380 (vs), 1306 (w), 1288 (w), 974 (s), 733 (s), 721 (vs), 661 (w).

Synthesis of HD/THTP_Cl. The hybrid nanodoughnut (DMA₄-HD, 0.36 g, 0.1 mmol, 1.0 eq.) was added in trihexyltetradecylphosphonium chloride (THTP_Cl, 5.19 g, 10 mmol, 100.0 eq.). The obtained mixtures were vigorously stirred at room temperature. The resulting green solution was added 5 mL acetonitrile and centrifuged to remove the precipitation. Finally, a green liquid was collected after rotary evaporation to remove acetonitrile.

Structural analysis. Powder x-ray diffraction (PXRD) patterns of the samples were collected at 40 kV and 40 mA on a Rigaku SmartLab diffractometer with Cu K α ($\lambda = 1.5416 \text{ \AA}$) radiation with 10°/min scan speed of and 0.02° in 2 θ step size. ¹H NMR spectrum was obtained on a Bruker 400 MHz spectrometer using D₂O as solvent. Mass spectrum was obtained using an Agilent 6530 Q-TOF mass spectrometer in positive-ion detection mode. Dynamic Light Scattering (DLS) measurements were performed using a Zetasizer Nano ZS90 under 2 min thermal equilibrium. Elemental analysis was performed on elemental vario EL cube. High-pressure CH₄ adsorption data were collected using a gravimetric sorption analyzers-isoSORP[®], from Rubotherm-TA instrument at 25 °C and a pressure range of 0–65 bar. MALDI-TOF mass spectrum were recorded on a Bruker UltrafleXtreme using DCTB as a matrix.

High-pressure methane absorption. The methane uptakes were collected in a magnetic suspension balance (isoSORP from Rubotherm-TA[®]) at 25 °C and a pressure range of 0–65 bar. The absorption chamber was loaded with ca. 0.5 g of liquid sample residing the sample bucket. The sample was then evacuated at 50 °C under vacuum to remove any traces of dissolved gases until the weight remained constant. The chamber was then pressurized with dry methane at 25 °C, and the weight change was traced by a magnetic suspension balance. Each step with different pressures took around 40 mins before equilibrium.

Thermal analysis. Thermal gravimetric analysis (TGA) was performed on Mettler Toledo TGA/DSC from 25 °C to 650 °C at 10 °C/min under N₂ with a flow rate of 40 mL/min. Differential scanning calorimetry (DSC) measurements were taken under N₂ atmosphere in the temperature range from –85 to 80 °C at a heating rate of 10 °C/min by using the DSC Q-20 TA instrument. To remove the thermal history, samples were pre-cooled from 25 to –85 °C, then reheated from –85 to 80 °C to collect data.

Rheologic analysis. Rheological properties were studied using Anton Paar MCR302. Strain-dependent and frequency-dependent rheology measurements were test by equipping CP25-2-SN27479 with a gap of 0.104 mm at room temperature. For temperature-dependent viscosity and stress versus shear rate measurements were test by equipping PP25-SN27504 with a gap of 0.100 mm under rotation mode.

Extraction experiments. Typically, 0.10 mL of HD/THTP_Cl was mixed with 2.0 mL of L-Trp aqueous solution (0.05 mol/L) followed by vigorous stirring for 8 h at room temperature. The amino acids uptake were determined using an Agilent 1260 Infinity II Prime LC system equipped with G1311 Quatpump, G1314F wavelength detector and Agilent ZORBAX SB-C18 column (150 mm \times 4.6 mm i.d., 5 μm particles). Amino acids were detected at specific wavelengths: 258 nm for L-Phe, 280 nm for L-Trp and L-Tyr. The mobile phase was composed of potassium dihydrogen phosphate aqueous solution (8 mmol/L) and HPLC-grade methanol with volumetric ratio of 9:1. The flow rate was set at 0.5 mL/min. The saccharides uptake were determined using an Agilent 1260 Infinity II Prime LC system equipped with an Agilent ZORBAX NH₂ column (150 \times 4.6 mm i.d., 5 μm particles) and a refractive index detector. The acetonitrile/water mixture (80/20, v/v) was used as the eluent. Calibration curve of amino acid were presented in Supplementary Figures. Extraction experiments were carried out in triplicate.

The Amino acid separation factor S_{ij} was calculated according to Eq. (1):

$$S_{ij} = (x_i/x_j)/(y_i/y_j) \quad (1)$$

where x is the mole fraction in HD/THTP_Cl phase, y is the mole fraction in the aqueous phase at equilibrium, i represents L-Trp, and j represents any other amino acid, respectively.

Structure unit occupation was calculated according to Eq. (2):

$$\text{Structure unit occupation} = q_e \times M \quad (2)$$

where q_e is the gravimetric uptake of amino acids that are immobilized by either HD cage or MOF structure (mol/g), M is the molecular weight of one HD cage or the molecular weight contained in one unit cell of MOF structure (g/mol). $M_{\text{HD}} = 3412.9$ g/mol, $M_{\text{MIL-140B}} = 2571.2$ g/mol, $M_{\text{MIL-140C}} = 2779.5$ g/mol, $M_{\text{MIL-140D}} = 3554.7$ g/mol, $M_{\text{MIL-68(AI)}} = 2497.3$ g/mol, $M_{\text{UIO-66}} = 1726.4$ g/mol, $M_{\text{MOF-808}} = 1387.5$ g/mol, $M_{\text{HY}} = 11530.8$ g/mol

Computational details. All the all-atom MD simulations were based on a gromos54a7 force field⁵⁵ by Automated Topology Builder (ATB)⁵⁶ and were carried out using the Gromacs-4.6.7 software package⁵⁷. The system is a relaxed liquid configuration at 298 K. The total run time was 10 ns NPT for the equilibrium MD simulation. We used the relaxed system as a starting configuration. As it is prior to system relaxation MD, energy minimization was carried out with a composite protocol of steepest descent using termination gradients of 100 kJ/mol-nm. The Nose-Hoover thermostat⁵⁸ was used to maintain the equilibrium temperature at 298 K and periodic boundary conditions were imposed on all three dimensions. The Particle Mesh-Ewald method^{59,60} was used to compute long-range electrostatics within a relative tolerance of 1×10^{-6} . A cut-off distance of 1 nm was applied to real-space Ewald interactions. The same value was used for van der Waals interactions. The LINCS algorithm⁶¹ was applied to constrain bond lengths of hydrogen atoms. A leap-frog algorithm⁶² was used with a time step of 2 fs. The wave function were generated with the GFN-xTB method⁶³ using xtb 6.3 software. The structure of the input xtb software comes from the equilibrium state in the MD simulation. Calculation of reduced density gradient⁵⁰ and second largest eigenvalue of the electron density hessian (λ_2) were performed in Multiwfn 3.7 program⁵². The molecular structures can be visualized through visual molecular dynamics software (VMD, version 1.9.3)⁶⁴. The binding energies were calculated by utilizing the g_mmpbsa⁶⁵ of GROMACS.

Data availability

All data that support the findings of this study are available within the paper and its Supplementary Information or from the corresponding author upon request. Source data are provided with this paper.

Received: 26 October 2021; Accepted: 12 April 2022;

Published online: 29 April 2022

References

- Giri, N. et al. Liquids with permanent porosity. *Nature* **527**, 216–220 (2015).
- Fulvio, P. F. & Dai, S. Porous liquids: the next frontier. *Chem.* **6**, 3263–3287 (2020).
- Jie, K., Zhou, Y., Ryan, H. P., Dai, S. & Nitschke, J. R. Engineering permanent porosity into liquids. *Adv. Mater.* **33**, 2005745 (2021).
- Ma, L. et al. Coordination cages as permanently porous ionic liquids. *Nat. Chem.* **12**, 270–275 (2020).
- Zhang, J. et al. Porous liquids: a promising class of media for gas separation. *Angew. Chem. Int. Ed.* **54**, 932–936 (2015).
- Gaillac, R. et al. Liquid metal–organic frameworks. *Nat. Mater.* **16**, 1149–11564 (2017).
- Chen, H. et al. A bifunctional zeolitic porous liquid with incompatible Lewis pairs for antagonistic cascade catalysis. *Chem.* **7**, 3340–3358 (2021).
- Li, P. et al. Electrostatic-assisted liquefaction of porous carbons. *Angew. Chem. Int. Ed.* **56**, 14958–14962 (2017).
- Shan, W. et al. New class of type III porous liquids: a promising platform for rational adjustment of gas sorption behavior. *ACS Appl. Mater. Interfaces* **10**, 32–36 (2018).
- Shi, T. et al. Effect of pore size on the carbon dioxide adsorption behavior of porous liquids based on hollow silica. *ChemPhysChem* **19**, 130–137 (2018).
- Kearsey, R. J., Alston, B. M., Briggs, M. E., Greenaway, R. L. & Cooper, A. I. Accelerated robotic discovery of type II porous liquids. *Chem. Sci.* **10**, 9454–9465 (2019).
- Kumar, R., Dhasaiyan, P., Naveenkumar, P. M. & Sharma, K. P. A solvent-free porous liquid comprising hollow nanorod–polymer surfactant conjugates. *Nanoscale Adv.* **1**, 4067–4075 (2019).
- He, S. et al. General way to construct micro- and mesoporous metal–organic framework-based porous liquids. *J. Am. Chem. Soc.* **141**, 19708–19714 (2019).
- Egleston, B. D. et al. Controlling gas selectivity in molecular porous liquids by tuning the cage window size. *Angew. Chem. Int. Ed.* **59**, 7362–7366 (2020).
- Cahir, J. et al. Type 3 porous liquids based on non-ionic liquid phases—a broad and tailorable platform of selective, fluid gas sorbents. *Chem. Sci.* **11**, 2077–2084 (2020).
- Mow, R. E. et al. Colloidal three-dimensional covalent organic frameworks and their application as porous liquids. *J. Mater. Chem. A* **8**, 23455–23462 (2020).
- Knebel, A. et al. Solution processable metal–organic frameworks for mixed matrix membranes using porous liquids. *Nat. Mater.* **19**, 1346–1353 (2020).
- Deng, Z. et al. Facilitate gas transport through metal–organic polyhedra constructed porous liquid membrane. *Small* **16**, 1907016 (2020).
- Lai, B. et al. Type 3 porous liquids for the separation of ethane and ethene. *ACS Appl. Mater. Interfaces* **13**, 932–936 (2021).
- Wang, D. et al. A universal approach to turn UiO-66 into type 1 porous liquids via post-synthetic modification with corona-canopy species for CO₂ capture. *Chem. Eng. J.* **416**, 127625 (2021).
- Hemming, E. B., Masters, A. F. & Maschmeyer, T. Exploring opportunities for platinum nanoparticles encapsulated in porous liquids as hydrogenation catalysts. *Chem.—A Eur. J.* **26**, 7059–7064 (2020).
- Cao, R. et al. Porous metal–organic framework liquids for enhanced CO₂ adsorption and catalytic conversion. *Angew. Chem. Int. Ed.* **60**, 20915–20920 (2021).
- Bhattacharjee, A., Kumar, R. & Sharma, K. P. Composite porous liquid for recyclable sequestration, storage and in situ catalytic conversion of carbon dioxide at room temperature. *ChemSusChem* **14**, 3303–3314 (2021).
- Giri, N. et al. Alkylated organic cages: from porous crystals to neat liquids. *Chem. Sci.* **3**, 2153–2157 (2012).
- Melaugh, G., Giri, N., Davidson, C. E., James, S. L. & Pópolo, M. G. D. Designing and understanding permanent microporosity in liquids. *Phys. Chem. Chem. Phys.* **16**, 9422–9431 (2014).
- Jie, K. et al. Transforming porous organic cages into porous ionic liquids via a supramolecular complexation strategy. *Angew. Chem. Int. Ed.* **59**, 2268–2272 (2020).
- Gosselin, A. J., Rowland, C. A. & Bloch, E. D. Permanently microporous metal–organic polyhedra. *Chem. Rev.* **120**, 8987–9014 (2020).
- Iv, J. J. P., Perman, J. A. & Zaworotko, M. J. Design and synthesis of metal–organic frameworks using metal–organic polyhedra as supermolecular building blocks. *Chem. Soc. Rev.* **38**, 1400–1417 (2009).
- Lee, S., Jeong, H., Nam, D., Lah, M. S. & Choe, W. The rise of metal–organic polyhedra. *Chem. Soc. Rev.* **50**, 528–555 (2021).
- Desiraju, G. R. *Crystal Engineering: The Design of Organic Solids* (Elsevier, 1989).
- Moulton, B. & Zaworotko, M. J. From molecules to crystal engineering: supramolecular isomerism and polymorphism in network solids. *Chem. Rev.* **101**, 1629–1658 (2001).
- Zhang, D., Ronson, T. K., Zou, Y.-Q. & Nitschke, J. R. Metal–organic cages for molecular separations. *Nat. Rev. Chem.* **5**, 168–182 (2021).
- Zhang, X. et al. Fine-tuning apertures of metal–organic cages: encapsulation of carbon dioxide in solution and solid state. *J. Am. Chem. Soc.* **141**, 11621–11627 (2019).
- Zhang, Z., Gao, W., Wojtas, L., Zhang, Z. & Zaworotko, M. J. A new family of anionic organic-inorganic hybrid doughnut-like nanostructures. *Chem. Commun.* **51**, 9223–9226 (2015).
- Murray, J., Kim, K., Ogoshi, T., Yao, W. & Gibb, B. C. The aqueous supramolecular chemistry of cucurbit[n]urils, pillar[n]arenes and deep-cavity cavitands. *Chem. Soc. Rev.* **46**, 2479–2496 (2017).
- Wang, Y. et al. Cyclodextrin porous liquid materials for efficient chiral recognition and separation of nucleosides. *ACS Appl. Mater. Interfaces* **12**, 45916–45928 (2020).
- Brand, M. C. et al. Melt-quenched porous organic cage glasses. *J. Mater. Chem. A* **9**, 19807–19816 (2021).
- Li, X. et al. Zeolitic imidazolate frameworks-based porous liquids with low viscosity for CO₂ and toluene uptakes. *Chem. Eng. J.* **417**, 129239 (2021).
- Greenaway, R. L. et al. Understanding gas capacity, guest selectivity, and diffusion in porous liquids. *Chem. Sci.* **8**, 2640–2651 (2017).
- Capela, E. V., Quental, M. V., Domingues, P., Coutinho, J. A. P. & Freire, M. G. Effective separation of aromatic and aliphatic amino acid mixtures using ionic-liquid-based aqueous biphasic systems. *Green. Chem.* **19**, 1850–1854 (2017).
- Vikramachakravarthi, D., Kumar, R. & Pal, P. Production of L (+) glutamic acid in a fully membrane-integrated hybrid reactor system: direct and continuous production under non-neutralizing conditions. *Ind. Eng. Chem. Res.* **53**, 19019–19027 (2014).
- Cooper, A. I. Porous molecular solids and liquids. *ACS Cent. Sci.* **3**, 544–553 (2017).
- Li, P. et al. Porous liquid zeolites: hydrogen bonding-stabilized H-ZSM-5 in branched ionic liquids. *Nanoscale* **11**, 1515–1519 (2019).
- Asghar, M. A. et al. Reversible phase transition triggered by order–disorder transformation of carboxyl oxygen atoms coupled with distinct reorientations in [HN(C₄H₉)₃](fumrate)_{0.5}(fumaric acid)_{0.5}. *Cryst. Growth Des.* **16**, 895–899 (2016).

45. Xu, Y., Zheng, Q. & Song, Y. Comparison studies of rheological and thermal behaviors of ionic liquids and nanoparticle ionic liquids. *Phys. Chem. Chem. Phys.* **17**, 19815–19819 (2015).
46. Althuluth, M., Kroon, M. C. & Peters, C. J. High pressure solubility of methane in the ionic liquid 1-hexyl-3-methylimidazolium tricyanomethanide. *J. Supercrit. Fluids* **128**, 145–148 (2017).
47. Anthony, J. L., Maginn, E. J. & Brennecke, J. F. Solubilities and thermodynamic properties of gases in the ionic liquid 1-n-butyl-3-methylimidazolium hexafluorophosphate. *J. Phys. Chem. B* **106**, 7315–7320 (2002).
48. Kostova, A. & Bart, H. J. Equilibrium study of amino acid reactive sorption with solvent impregnated resins, part I. *Solvent Extraction Ion. Exch.* **25**, 109–126 (2007).
49. Zhou, Y. et al. Integrated, one-pot carbon capture and utilisation using porous ionic liquids. *Chem. Commun.* **57**, 7922–7925 (2021).
50. Johnson, E. R. et al. Revealing noncovalent interactions. *J. Am. Chem. Soc.* **132**, 6498–6506 (2010).
51. Jonckheere, D. et al. Adsorption and separation of aromatic amino acids from aqueous solutions using metal–organic frameworks. *ACS Appl. Mater. Interfaces* **9**, 30064–30073 (2017).
52. Lu, T. & Chen, F. Multiwfn: a multifunctional wavefunction analyzer. *J. Comput. Chem.* **33**, 580–592 (2012).
53. Xiao, H. et al. Synergistic combination of the capillary effect of collagen fibers and size-sieving merits of metal–organic frameworks for emulsion separation with high flux. *Ind. Eng. Chem. Res.* **59**, 14925–14934 (2020).
54. Li, X., Zhao, D. & Zheng, S. Recent advances in POM-organic frameworks and POM-organic polyhedra. *Coord. Chem. Rev.* **397**, 220–240 (2019).
55. Christen, M. et al. The GROMOS software for biomolecular simulation: GROMOS05. *J. Comput. Chem.* **26**, 1719–1751 (2005).
56. Canzar, S. et al. Charge group partitioning in biomolecular simulation. *J. Comput. Biol.* **20**, 188–198 (2013).
57. Hess, B., Kutzner, C., van der Spoel, D. & Lindahl, E. GROMACS 4: algorithms for highly efficient, load-balanced, and scalable molecular simulation. *J. Chem. Theory Comput.* **4**, 435–447 (2008).
58. Berendsen, H. J. C., Postma, J. P. M., van Gunsteren, W. F., DiNola, A. & Haak, J. R. Molecular dynamics with coupling to an external bath. *J. Chem. Phys.* **81**, 3684–3690 (1984).
59. Astrakas, L. G., Gousias, C. & Tzaphlidou, M. Structural destabilization of chignolin under the influence of oscillating electric fields. *J. Appl. Phys.* **111**, 074702 (2012).
60. Essmann, U. et al. A smooth particle mesh Ewald method. *J. Chem. Phys.* **103**, 8577–8593 (1995).
61. Hess, B., Bekker, H., Berendsen, H. J. C. & Fraaije, J. G. E. M. LINCS: a linear constraint solver for molecular simulations. *J. Comput. Chem.* **18**, 1463–1472 (1997).
62. Van Gunsteren, W. F. & Berendsen, H. J. C. A leap-frog algorithm for stochastic dynamics. *Mol. Simul.* **1**, 173–185 (1988).
63. Grimme, S., Bannwarth, C. & Shushkov, P. A robust and accurate tight-binding quantum chemical method for structures, vibrational frequencies, and noncovalent interactions of large molecular systems parametrized for all spd-block elements ($z = 1–86$). *J. Chem. Theory Comput.* **13**, 1989–2009 (2017).
64. Humphrey, W., Dalke, A. & Schulten, K. VMD: visual molecular dynamics. *J. Mol. Graph.* **14**, 33–38 (1996).
65. Kumari, R., Kumar, R., Consortium, O. S. D. D. & Lynn, A. g_mmpbsa—a GROMACS tool for high-throughput MM-PBSA calculations. *J. Chem. Inf. Model.* **54**, 1951–1962 (2014).

Acknowledgements

The authors gratefully acknowledge the financial support from the National Key R&D Program of China (2021YFE0191100, Z.Z.), the National Natural Science Foundation of China (21808104 and 21676141 to Z.Z. and J.T.), and Key R&D Program of Jiangsu Province (BE2021710, Xu Qiao).

Author contributions

Z.Z.: Conceptualization, Investigation, Writing—original draft, Writing—review & editing. B.Y.: Simulation, Writing—original draft, Validation, Software, Visualization. B.Z.: Investigation, Methodology, Data analysis. M.C.: Simulation, Data analysis, Validation. J.T.: Supervision, Writing—review & editing. X.Q.: Project administration, Funding acquisition.

Competing interests

The authors declare no competing interests.

Additional information

Supplementary information The online version contains supplementary material available at <https://doi.org/10.1038/s41467-022-30092-2>.

Correspondence and requests for materials should be addressed to Jihai Tang or Xu Qiao.

Peer review information *Nature Communications* thanks Jocasta Avila and the other, anonymous, reviewer(s) for their contribution to the peer review of this work.

Reprints and permission information is available at <http://www.nature.com/reprints>

Publisher's note Springer Nature remains neutral with regard to jurisdictional claims in published maps and institutional affiliations.



Open Access This article is licensed under a Creative Commons Attribution 4.0 International License, which permits use, sharing, adaptation, distribution and reproduction in any medium or format, as long as you give appropriate credit to the original author(s) and the source, provide a link to the Creative Commons license, and indicate if changes were made. The images or other third party material in this article are included in the article's Creative Commons license, unless indicated otherwise in a credit line to the material. If material is not included in the article's Creative Commons license and your intended use is not permitted by statutory regulation or exceeds the permitted use, you will need to obtain permission directly from the copyright holder. To view a copy of this license, visit <http://creativecommons.org/licenses/by/4.0/>.

© The Author(s) 2022